BEILSTEIN ARCHIVES

This open access document is posted as a preprint in the Beilstein Archives at https://doi.org/10.3762/bxiv.2026.43.v1 and is considered to be an early communication for feedback before peer review. Before citing this document, please check if a final, peer-reviewed version has been published.

This document is not formatted, has not undergone copyediting or typesetting, and may contain errors, unsubstantiated scientific claims or preliminary data.

Preprint Title	Downsizing NiCoS Pentlandite by Laser Fragmentation in Liquids for Enhanced HER Performance
Authors	Philipp Lemm, Janna Wierper, Oleg Prymak, Kateryna Loza, Julian Kleinhaus, Ulf-Peter Apfel and Benjamin Mockenhaupt
Publication Date	02 Nov 2026
Article Type	Full Research Paper
Supporting Information File 1	SI_NiCoS_BJNANO_Submission.docx; 3.3 MB
ORCID® iDs	Philipp Lemm - https://orcid.org/0009-0000-7426-2669; Oleg Prymak - https://orcid.org/0000-0002-9494-8411; Julian Kleinhaus - https://orcid.org/0000-0002-0901-4789; Benjamin Mockenhaupt - https://orcid.org/0000-0001-8054-8698

License and Terms: This document is copyright 2026 the Author(s); licensee Beilstein-Institut.

This is an open access work under the terms of the Creative Commons Attribution License (https://creativecommons.org/licenses/by/4.0). Please note that the reuse, redistribution and reproduction in particular requires that the author(s) and source are credited and that individual graphics may be subject to special legal provisions.
The license is subject to the Beilstein Archives terms and conditions: https://www.beilstein-archives.org/xiv/terms.
The definitive version of this work can be found at https://doi.org/10.3762/bxiv.2026.43.v1

Downsizing NiCoS Pentlandite by Laser Fragmentation in Liquids for Enhanced HER Performance

Philipp Lemm[1], Janna Wierper[2,4], Oleg Prymak[3], Kateryna Loza[3], Julian Kleinhaus[4], Ulf-Peter Apfel[2,4] and Benjamin Mockenhaupt[1*]

[1]Technical Chemistry I, University of Duisburg-Essen and Center for Nanointegration Duisburg-Essen (CENIDE), Universitätsstraße 7, 45141 Essen, Germany.

[2]Department Power to Chemicals, Fraunhofer Institute for Environmental, Safety and Energy Technology UMSICHT, Osterfelder Str. 3, 46047 Oberhausen, Germany.

[3]Inorganic Chemistry, University of Duisburg-Essen, Universitätsstraße 7, Essen 45141, Germany.

[4]Activation of Small Molecules/ Technical Electrochemistry, Ruhr University Bochum, Universitätsstraße 150, 44801 Bochum, Germany.

Benjamin Mockenhaupt – benjamin.mockenhaupt@uni-due.de

Abstract

Pentlandites have demonstrated promising hydrogen evolution reaction (HER) performance and are particularly attractive due to their earth abundance and direct utilization as naturally occurring ores. However, their micrometer-scale particle size limits the accessible surface area and effective catalyst utilization. Laser fragmentation in liquids (LFL) offers an approach to overcome this limitation by producing nanoparticles while largely preserving the structure and composition of the pristine material. Therefore, picosecond LFL was employed to fragment $Ni_{2.25}Co_{6.75}S_8$ pentlandite microparticles into nanoparticles with the aim of enhancing their HER performance. By systematically varying the laser fluence (200-800 mJ/cm²) and the induced pulses per volume (24-72 PPV), optimal fragmentation conditions were identified, while the resulting structural and chemical composition as well as the HER performance were comprehensively investigated using electron microscopy, X-ray diffraction, energy-dispersive X-ray spectroscopy, thermogravimetric analysis, electron paramagnetic resonance spectroscopy, and electrochemical characterization. The microparticles were successfully fragmented into 10-40 nm nanoparticles while largely preserving their crystal structure, however with indications of composition changes at higher fluences. Laser processing at fluences of ≥600 mJ/cm² reduced the HER overpotential by up to 50 mV (≈15%) compared to the pristine material. This enhancement is most likely associated with the formation of a thin carbon shell and an increased concentration of paramagnetic species, indicating a higher defect density in the laser-fragmented nanoparticles. The laser-fragmented catalysts were further successfully integrated into a zero-gap electrolyzer, demonstrating their applicability under a technologically relevant reaction environment. This approach demonstrates the potential of LFL as a promising tool for converting micrometer-sized catalyst

powders into nanostructured materials while preserving their crystal structure and improving their catalytic performance, thereby enabling catalyst optimization beyond the capabilities of conventional processing methods.

Keywords

Energy Storage; Hydrogen Evolution Reaction; Laser Fragmentation in Liquids; Nanoparticle Synthesis; Pentlandite

Introduction

The transition toward a sustainable energy economy relies on the large-scale deployment of renewable energy sources and efficient energy storage technologies, with green hydrogen emerging as a key energy carrier for the decarbonization of future energy systems. [1–4] Among the available hydrogen production technologies, proton exchange membrane (PEM) water electrolysis is currently considered one of the most promising approaches. [5–7] However, its widespread implementation is still limited by the reliance on expensive and scarce platinum-group metal catalysts. Consequently, the development of earth-abundant alternatives capable of delivering competitive activity and stability has become a major research focus. Among the emerging alternatives to noble-metal catalysts, pentlandite-type sulfides have gained considerable attention for the hydrogen evolution reaction (HER) due to their competitive catalytic activity and stability in acidic media combined with their abundance and low cost. [8–10] Notably, these minerals constitute a major natural source of nickel and thus are naturally abundant with different compositions. Consequently, sufficiently pure deposits can be mined at low cost and used with minimal further processing, although with non-uniform µm-ranged particle sizes and

varying Fe : Ni contents.[11] Subsequently, a broad range of synthetic pentlandite-type sulfides, including NiFeS [12, 13], NiCoS [9, 14], and NiCoFeS [8, 15] compositions, were already investigated and have demonstrated promising HER and oxygen evolution reaction (OER) performance, highlighting the potential of this material class. Despite these advantages, the catalytic performance of pentlandite materials may still be limited by the relatively large particle sizes commonly obtained through conventional synthesis and processing routes.[16] Reducing particle size is expected to increase the accessible surface area and improve catalyst utilization. However, established top-down approaches such as mechanical ball milling typically remain restricted to the hundreds of nanometers and the lower micrometer regime and do not readily provide access to well-defined pentlandite nanoparticles. [12, 10] To overcome these limitations, alternative particle downsizing strategies capable of producing nanoscale pentlandite while preserving its composition and structural integrity are required. In this context, LFL has emerged as a versatile and contamination-free technique for the production of nanomaterials through the controlled downsizing of suspended microparticles. [17] LFL has successfully been applied to a broad range of material classes, including Au [18], ZnO and B_4C microparticles [19], pharmaceuticals [20], and organic compounds such as curcumin. [21] Furthermore, the laser-induced downsizing of IrO_2 [22] and Co_3O_4[23] microparticles has been reported to enhance electrocatalytic performance toward the OER, suggesting it may also be beneficial for improving the catalytic performance of pentlandite-based HER catalysts. Importantly, LFL is not limited to laboratory-scale investigations, as continuous-flow processing concepts have already demonstrated nanoparticle production rates on the order of 10 g/h, highlighting the scalability and technological relevance of this approach. [24]

Motivated by these considerations, the present work investigates the laser fragmentation of $Ni_{2.25}Co_{6.75}S_8$ pentlandite microparticles in a liquid round jet to

generate nanoscale catalysts (Figure 1) and evaluate the potential of particle downsizing as a strategy to enhance HER performance. To preserve the crystal structure and chemical composition of the material, fragmentation was performed using picosecond laser pulses, which promote photomechanical fragmentation while reducing thermal energy transfer compared to nanosecond processing, thereby minimizing melting and oxidation processes. [25] Furthermore, a wavelength of 1064 nm was chosen due to its greater optical penetration depth compared to visible and ultraviolet wavelengths, enabling more homogeneous energy deposition within the microparticles and thus facilitating efficient bulk fragmentation. Isopropanol was chosen as the fragmentation medium owing to its efficient radical-scavenging properties [26], which minimize oxidation during laser processing, and because alcohols have been reported to form the thinnest carbon shells among commonly used organic solvents in laser-based nanoparticle synthesis. [27] Based on this approach, a systematic study varying the laser fluence (200, 400, 600, and 800 mJ/cm^2) and the induced laser pulses per volume (24, 48, and 72 PPV) was conducted. The selected laser fluence range is consistent with previous studies on picosecond laser fragmentation of microparticles in liquids [28, 29], while the applied pulse exposure was systematically varied to investigate its influence on particle fragmentation and catalytic performance. The resulting particles were subsequently characterized with respect to their size, composition, and HER performance in a standard H-type cell as well as a zero-gap PEM setup in order to identify the optimal laser processing parameters for efficient pentlandite fragmentation.

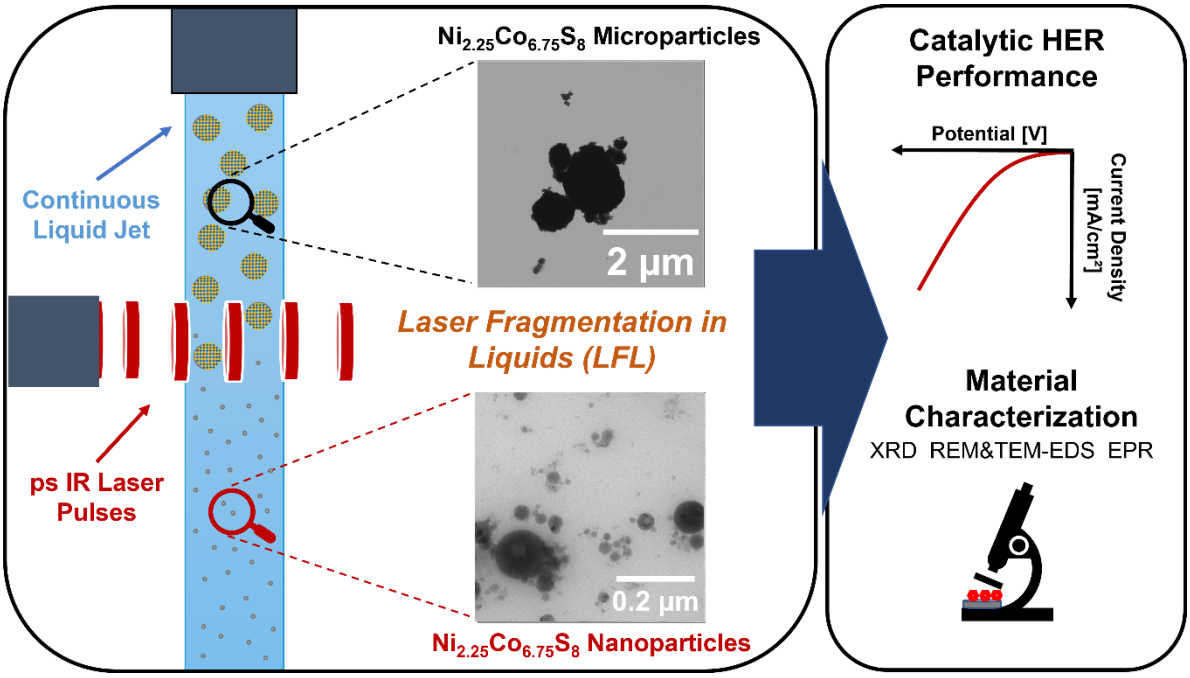


Figure 1: Schematic overview of the experimental design used to evaluate the fragmentation of $Ni_{2.25}Co_{6.75}S_8$ pentlandite microparticles.

The results demonstrate successful fragmentation of the $Ni_{2.25}Co_{6.75}S_8$ pentlandite microparticles for all investigated laser fluences, with TEM analysis revealing efficient particle downsizing into the tenth-nanoscale regime. While laser processing at 200 mJ/cm² results in only partial fragmentation, fluences of 400 mJ/cm² and above lead to essentially complete fragmentation of the microparticles into nanoparticles, with no significant differences in particle size observed upon further increasing the laser fluence. While XRD demonstrates that the pentlandite crystal structure is largely retained during laser processing, SEM-EDS measurements reveal compositional changes at laser fluences of ≥400 mJ/cm² and ≥48 PPV, evidenced by a progressive decrease in the sulfur content. Interestingly, substantial improvements in HER activity are observed primarily for samples processed at 600 and 800 mJ/cm², accompanied by enhanced electrochemical stability. Since these performance gains cannot be explained solely by particle size reduction, additional characterization was performed.

EPR measurements reveal an increased concentration of paramagnetic species in samples processed at higher fluences, indicating an elevated defect density, which is widely recognized to promote electrocatalytic activity. [30–33] Furthermore, TEM-EDS analyses suggest the possible presence of thin carbon surface layers formed during laser processing, which may additionally contribute to the enhanced HER performance, consistent with previous reports on carbon-coated electrocatalysts. [34] The study demonstrates that LFL provides an effective route toward nanoscale pentlandite catalysts and establishes a foundation for further optimization of earth-abundant HER materials through laser-based nanostructuring.

Results and Discussion

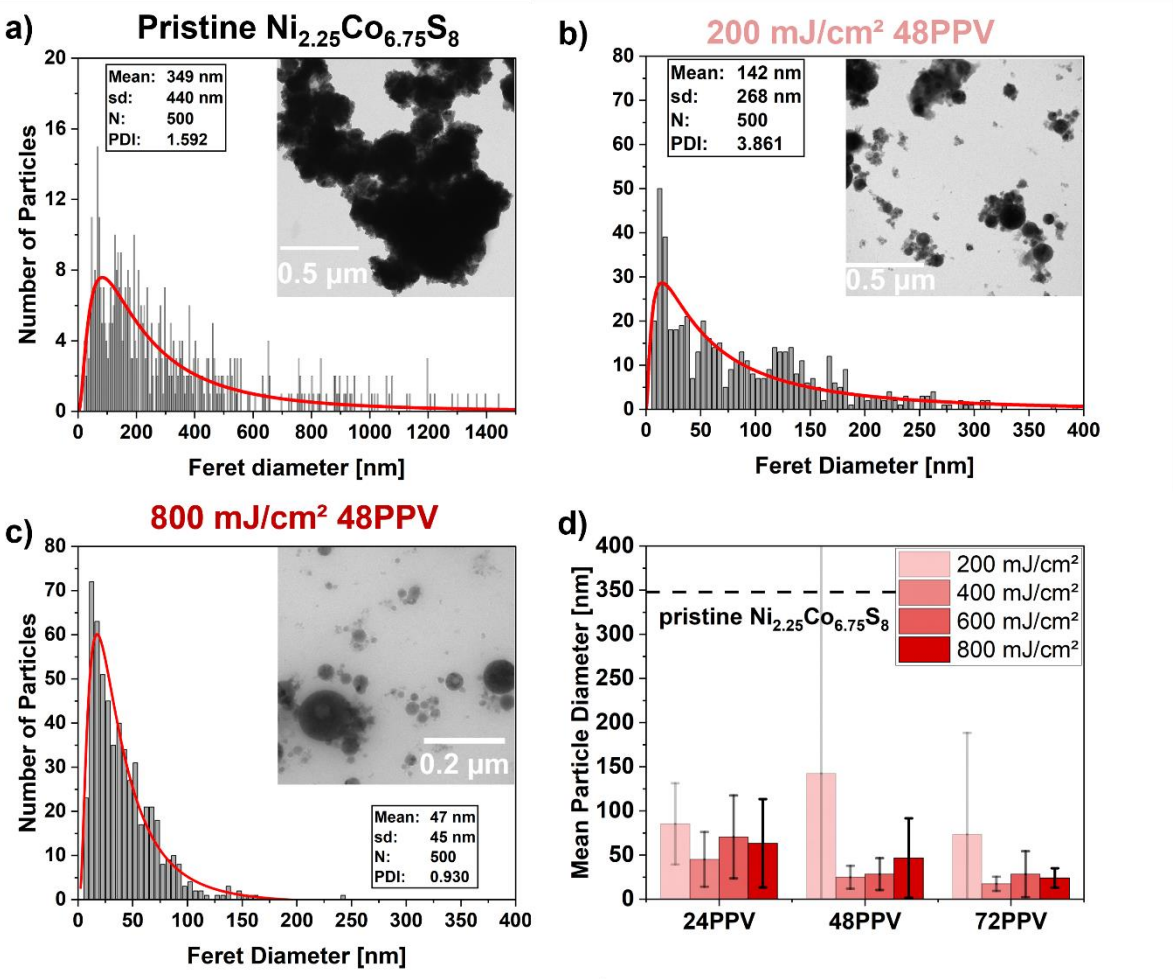


Figure 2: Representative TEM micrographs and corresponding number-based particle size distributions of $Ni_{2.25}Co_{6.75}S_8$ pentlandite particles: (a) pristine material, (b) sample processed at 200 mJ/cm² and 48 PPV, and (c) sample processed at 800 mJ/cm² and 48 PPV. (d) Mean particle diameters determined from statistical TEM analysis of 500 particles for all investigated laser fluences and PPV.

The influence of picosecond laser processing on the morphology and particle size of $Ni_{2.25}Co_{6.75}S_8$ pentlandite particles was first investigated by transmission electron microscopy (TEM). Representative TEM micrographs together with the corresponding

particle size distributions are shown in Figure 2a-c, illustrating the morphological evolution from the pristine material to partially and completely fragmented particles. A quantitative comparison of all investigated laser fluences and Pulses per Volume (PPV) is provided by the mean particle diameters obtained from statistical TEM particle analysis (Figure 2d). The calculation of the PPV is described in Supporting Information Section S1. For each sample, 500 particles were evaluated to obtain statistically representative number-based particle size distributions. The complete TEM particle size distributions for all investigated processing conditions, from which the mean particle diameters shown in Figure 2d were derived, are provided in the Supporting Information (Figures S3-S6). The pristine $Ni_{2.25}Co_{6.75}S_8$ material exhibits a mean particle diameter of 348 nm with a standard deviation of 439 nm and a polydispersity index (PDI) of 1.592 (Figure 2a). The large standard deviation, exceeding the mean particle diameter, reflects the highly heterogeneous nature of the starting material, which contains particles spanning from the sub-micrometer to the micrometer size range. Following laser processing at 200 mJ/cm² and 48 PPV, the mean particle diameter decreases to 142 nm (Figure 2b), demonstrating that fragmentation is already initiated at the lowest investigated laser fluence. However, the large standard deviation of 268 nm together with the high PDI of 3.861 indicates that the particle population remains highly heterogeneous. The coexistence of newly formed nanoparticles and larger residual particles suggests that fragmentation is incomplete under these processing conditions. In contrast, processing at 800 mJ/cm² and 48 PPV results in a mean particle diameter of only 46 nm, accompanied by a standard deviation of 45 nm and a PDI of 0.930 (Figure 2c). The pronounced decrease in both the mean particle diameter and the PDI indicates substantially more extensive fragmentation and the formation of a considerably more homogeneous nanoparticle population compared with the pristine material and the sample processed at 200 mJ/cm². Besides the

influence of laser fluence, the induced PPV also has a pronounced effect on the fragmentation process (Fig. 2d). Increasing the number of PPV decreases the mean particle diameter, demonstrating that repeated laser-particle interactions progressively refine the remaining larger particles. This trend is particularly evident at 400 mJ/cm², where the mean particle diameter decreases from 45 nm after 24 PPV to 25 nm after 48 PPV and further to only 17 nm after 72 PPV. Furthermore, the distributions become progressively narrower with increasing PPV, indicating an increasingly monodisperse particle population (Figures S3-S7). Besides the pronounced reduction in particle size, the TEM micrographs reveal a distinct evolution of the particle morphology with increasing laser processing intensity. The pristine material is dominated by irregularly shaped particles with sharp edges and angular morphologies (Figure 2a). After processing at 200 mJ/cm² and 48 PPV, an increasing fraction of particles exhibits rounded morphologies, while irregular residual particles are still present (Figure 2b). In contrast, the sample processed at 800 mJ/cm² and 48 PPV consists almost exclusively of spherical nanoparticles (Figure 2c).

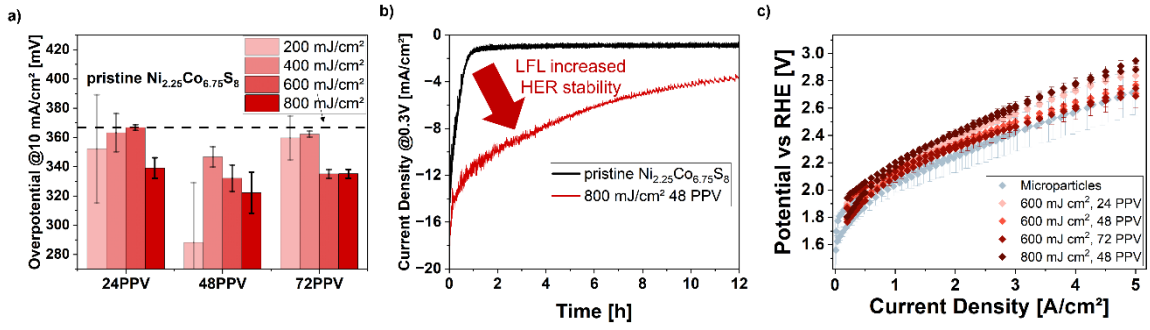


Figure 3: Electrochemical HER performance of pristine and laser-fragmented $Ni_{2.25}Co_{6.75}S_8$ pentlandite particles. (a) HER overpotential at a current density of 10 mA/cm² for all investigated laser fluences (200, 400, 600, and 800 mJ/cm²) and induced Pulses per Volume (24, 48, and 72 PPV). (b) Chronoamperometric stability measurements comparing the pristine $Ni_{2.25}Co_{6.75}S_8$ material with the sample

processed at 800 mJ/cm² and 48 PPV, which exhibited the highest HER activity in the RDE screening. (c) Zero-gap electrolyzer polarization curves of selected $Ni_{2.25}Co_{6.75}S_8$ pentlandite samples exhibiting enhanced HER activity in the RDE measurements, with the pristine microparticles included as a reference.[35]

Having established that picosecond laser processing enables efficient fragmentation of $Ni_{2.25}Co_{6.75}S_8$ pentlandite particles over a broad range of laser parameters, the resulting nanoparticles were subsequently evaluated for the hydrogen evolution reaction (HER). Figure 3a summarizes the HER overpotentials at a current density of 10 mA/cm² for all investigated conditions together with the pristine material. The corresponding polarization curves are provided in the Supporting Information (Figure S7). The pristine $Ni_{2.25}Co_{6.75}S_8$ exhibits an overpotential of approximately 368 mV at 10 mA/cm², which is in good agreement with the HER activity reported for comparable pentlandite-based catalysts in the literature. [9] The 200 mJ/cm² series shows considerably larger error bars compared to the other fluence series, which could be attributed to the incomplete fragmentation and the resulting heterogeneous particle population revealed by the TEM analysis. Consequently, the apparent improvement observed for the sample processed at 200 mJ/cm² and 48 PPV was not considered statistically significant and was therefore excluded from the statistical evaluation. Taking that into account, processing at 200 and 400 mJ/cm² for all investigated PPV results in only minor changes in the HER overpotential, indicating no significant improvement in HER performance. In contrast, samples processed at 600 and 800 mJ/cm² exhibit a pronounced improvement in HER performance, decreasing the overpotentials by 10-15 % to approximately 320-340 mV, depending on the PPV. Interestingly, the observed enhancement in HER activity does not correlate directly with the reduction in particle size. As demonstrated by the TEM analysis (Figure 2),

partial particle size reduction is already achieved at 200 mJ/cm², while processing at 400 mJ/cm² produces nanoparticles with mean diameters comparable to those obtained at 600 and 800 mJ/cm². These findings indicate that the increased electrochemically accessible surface area resulting from particle size reduction alone cannot account for the enhanced catalytic performance. Since the increase in geometric surface area resulting from particle size reduction does not necessarily correlate with the electrochemically active surface area (ECSA), double-layer capacitance measurements were performed for the pristine $Ni_{2.25}Co_{6.75}S_8$ microparticles and samples processed at 400 and 800 mJ/cm² 48 PPV to assess whether differences in electrochemically accessible surface area could explain the enhanced HER activity (Figure S8). Interestingly, the pristine material exhibited a capacitance of approximately 6 mF/cm², which decreased to approximately 4 and 3.4 mF/cm² after laser processing at 400 and 800 mJ/cm², respectively. These results indicate that the enhanced HER activity at higher laser fluences cannot be attributed to an increase in electrochemically accessible surface area. Instead, additional laser-induced modifications to the catalyst, beyond simple fragmentation, must contribute to the improved HER activity observed at higher laser fluences. The sample processed at 800 mJ/cm² and 48 PPV, exhibiting the highest HER activity, was selected for further electrochemical RDE characterization. Chronoamperometric measurements (Figure 3b) further demonstrate that the laser-fragmented sample not only exhibits higher HER activity but also improved electrochemical stability compared to the pristine $Ni_{2.25}Co_{6.75}S_8$. Although both electrodes display a gradual decrease in current density over time, the fragmented material consistently maintains higher cathodic currents throughout the measurement. It should be noted that stability measurements performed on RDE generally exhibit pronounced current decay due to substrate passivation. [36] This interpretation is in good agreement with previous studies on

laser-generated electrocatalysts, where laser-induced defects have likewise been associated with enhanced electrochemical performance. For example, laser-synthesized Ag nanoparticles exhibiting a high density of stacking faults showed significantly improved stability compared to the corresponding pristine material. [31] Similarly, laser fragmentation of IrO_2 has been reported to simultaneously enhance both catalytic activity and stability through laser-induced structural modifications. [28] Based on the RDE screening, the most promising samples, comprising the complete 600 mJ/cm² series together with the sample processed at 800 mJ/cm² and 48 PPV, were subsequently evaluated in a zero-gap electrolyzer to assess their performance under application-relevant conditions (Figure 3c). The resulting polarization curves reveal comparable overall cell voltages for all laser-fragmented samples and the pristine $Ni_{2.25}Co_{6.75}S_8$ catalyst. In contrast to the RDE measurements, which predominantly probe the intrinsic electrocatalytic HER kinetics under well-defined mass transport conditions, the performance of a zero-gap electrolyzer is additionally influenced by factors such as mass transport limitations, gas evolution, catalyst layer architecture, and cell resistances. [37] Consequently, improvements in the intrinsic catalytic activity do not necessarily translate directly into enhanced full-cell performance. Consistent with this observation, electrochemical impedance spectroscopy performed at current densities of 0.5 and 1.0 A/cm² (Figures S9a,b) does not reveal a significant reduction in the charge-transfer resistance for the laser-fragmented catalysts compared to the pristine material.

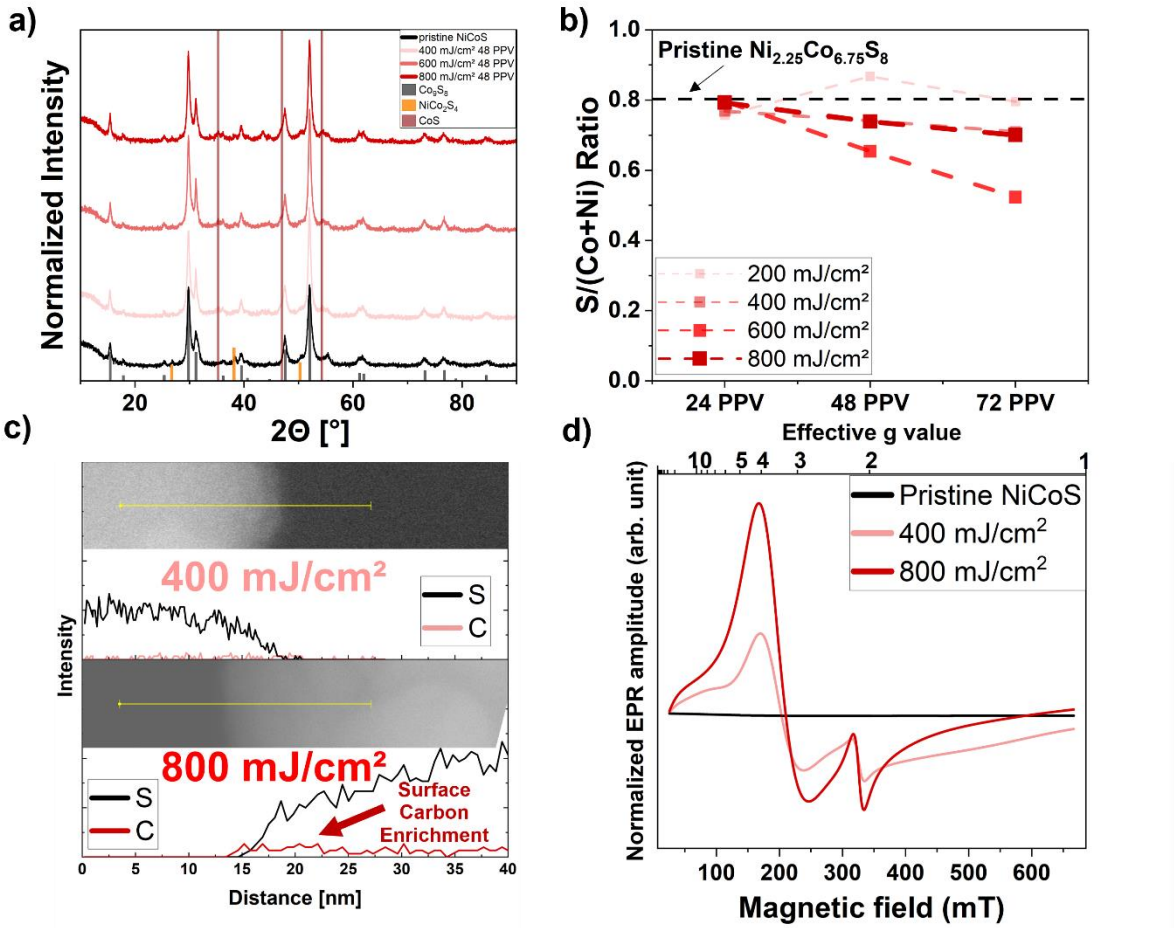


Figure 4: Structural and compositional characterization of selected laser-fragmented $Ni_{2.25}Co_{6.75}S_8$ pentlandite particles. (a) X-ray diffraction (XRD) patterns of the pristine material and samples processed at 400, 600, and 800 mJ/cm² with 48 PPV. (b) Sulfur-to-metal [S/(Co + Ni)] ratio, determined by SEM-EDS for all investigated laser fluences and PPV. (c) STEM-EDS line scan profiles of the samples processed at 400 and 800 mJ/cm² at 48 PPV. (d) Electron paramagnetic resonance (EPR) spectra of the pristine material and samples processed at 400 and 800 mJ/cm² at 48 PPV.

Although no significant improvement in the overall zero-gap electrolyzer performance was observed for the investigated $Ni_{2.25}Co_{6.75}S_8$ system, the intrinsic HER enhancement revealed by the RDE measurements highlights the potential of laser

fragmentation in liquids as a strategy for boosting catalyst performance. These findings encourage the application of LFL to other catalyst materials, where laser-induced structural modifications may translate more directly into improved device performance. Consequently, understanding the origin of the enhanced intrinsic catalytic activity is crucial for enabling the targeted introduction of these laser-induced modifications in future catalyst design. Therefore, selected samples were subjected to comprehensive structural and compositional analyses (Fig. 4) to identify the laser-induced material modifications responsible for the observed improvement in HER performance.

X-ray diffraction (XRD) was employed to determine whether the enhanced catalytic activity originates from laser-induced changes in the crystal structure. The corresponding diffraction patterns of the pristine $Ni_{2.25}Co_{6.75}S_8$ together with the samples processed at 400, 600, and 800 mJ/cm² at 48 PPV are shown in Figure 4a. These samples were selected because the electrochemical measurements revealed a distinct improvement in HER activity beginning at laser fluences of 600 mJ/cm², indicating a predominantly fluence-dependent rather than PPV-dependent effect. To not exclude PPV-dependent effects, XRD patterns of the entire 600 mJ/cm² PPV series were also investigated and are provided in the Supporting Information (Figure S10a). Overall, the diffraction patterns reveal no significant changes in the characteristic reflections of the pristine material upon laser processing, indicating that the crystalline structure is largely preserved without any clear evidence of amorphization. This observation is consistent with previous studies on picosecond laser processing in liquids, typically yielding crystalline rather than amorphous nanoparticles. [38] However, additional small diffraction peaks emerge after laser processing, which can be attributed to the formation of a minor CoS phase and are further analyzed and discussed in the following section.

The subsequent Rietveld refinement reveals subtle changes in the phase composition (Fig. S11). For the pristine $Ni_{2.25}Co_{6.75}S_8$, the diffraction pattern is predominantly described by a Co_9S_8-type phase (88 wt%), while a minor $NiCo_2S_4$ phase (12 wt%) is required to account for the remaining reflections. Following laser fragmentation, as mentioned, a small CoS phase is additionally detected in all processed samples. However, the CoS phase is detected in all laser-fragmented samples, including those processed at 400 mJ/cm² that exhibit no improvement in HER activity, indicating that its formation is unlikely to be responsible for the enhanced catalytic performance. Additionally, the laser processing reduces the $NiCo_2S_4$ phase fraction to approximately 5 wt%, accompanied by a corresponding increase in the Co_9S_8-type phase fraction to about 94 wt%. Notably, these changes are also already observed for samples processed at 400 mJ/cm², where no significant improvement in HER activity is detected, indicating that the observed variations in phase composition cannot explain the enhanced catalytic performance.

The crystallite sizes obtained from the Rietveld refinement are summarized in Figures S10d-f. For the pristine material, average crystallite sizes of approximately 13 nm and 15 nm were determined for the Co_9S_8- and $NiCo_2S_4$-type phases, respectively. These values are substantially smaller than the particle size of the pristine material, which is in the micro- to sub-micrometer range, as well as the average particle size of the laser-fragmented samples (~40 nm, TEM), demonstrating that both the pristine and laser-fragmented particles are polycrystalline rather than single-crystalline. Following laser processing, only a slight increase in crystallite size is observed for both phases, reaching approximately 16 nm for the Co_9S_8-type phase and 19 nm for the $NiCo_2S_4$-type phase (Fig. S10d-f). Notably, this increase is present for every laser treatment and shows no systematic dependence on either laser fluence or pulses per volume (PPV). Consequently, the modest crystallite growth does not correlate with the fluence-

dependent enhancement in HER activity and is therefore unlikely to be the origin of the improved catalytic performance.

The evolution of the lattice parameters is summarized in Figure S12. Only a slight lattice contraction is observed for the CoS phase, with the lattice parameter *a* decreasing from approximately 3.395 Å at 400 mJ/cm² to values ranging from 3.387 to 3.392 Å at 600 and 800 mJ/cm². Apart from this minor change, no clear systematic trends in the lattice parameters can be identified when comparing the sample processed at 400 mJ/cm² with those exhibiting enhanced HER activity at higher laser fluences (≥600 mJ/cm², 24 PPV). Thus, the lattice parameter analysis provides no clear evidence of substantial crystallographic differences between the laser-processed samples with unchanged HER activity and those exhibiting enhanced catalytic performance. Nevertheless, such subtle lattice contractions are consistent with the concept of pulsed laser defect engineering in liquids (PUDEL), for which laser-induced lattice distortions and defect formation have previously been demonstrated. [32, 39] While the observed changes alone do not provide direct evidence of defect formation, they suggest that laser-induced defects may contribute to the enhanced catalytic activity and therefore warrant further investigation using complementary characterization techniques.

To further investigate laser-induced compositional changes, SEM-EDS measurements were performed to determine the global elemental composition of the pristine and laser-fragmented particles. Figure 4b presents the sulfur-to-metal ratio, S/(Co+Ni), calculated from the measured sulfur, cobalt, and nickel contents, enabling a direct assessment of changes in the overall sulfur content as a function of laser processing. Figure S13 summarizes the individual Ni, Co, and S elemental fractions from which the sulfur-to-metal ratios were calculated. For the pristine $Ni_{2.25}Co_{6.75}S_8$ this corresponds to a sulfur-to-metal ratio of approximately 0.80. Interestingly, no measurable change in

the sulfur content is observed for samples processed with 24 PPV, irrespective of the applied laser fluence. Even at the highest investigated fluence of 800 mJ/cm², the sulfur-to-metal ratio remains essentially unchanged. Likewise, the complete 200 mJ/cm² PPV series exhibits a nearly constant sulfur-to-metal ratio. Consequently, these results provide no evidence for substantial oxidation of the particles. In contrast, a pronounced decrease in the sulfur-to-metal ratio is observed for the 400-800 mJ/cm² series at 48 and 72 PPV. Here, the sulfur-to-metal ratio decreases from approximately 0.80 for the pristine material to around 0.70 for the 400 and 800 mJ/cm² series and to approximately 0.55 for the 600 mJ/cm² series. This progressive decrease in sulfur content may be associated with partial oxidation of the particles during laser processing or the formation of sulfur vacancies, which are known to influence the catalytic properties of pentlandite and may therefore contribute to changes in HER activity. However, since sulfur depletion is already observed for the 400 mJ/cm² series, where no significant enhancement in HER activity is detected, sulfur loss alone cannot explain the improved catalytic performance at higher laser fluences. The potential role of sulfur vacancies is further discussed in the context of the EPR measurements presented later in this work. In addition to the Ni, Co, and S contents, the oxygen and carbon contents were determined by SEM-EDS to evaluate the formation and deposition of carbonaceous pyrolysis products or oxidized surface species (Fig. S14). Such laser-induced solvent decomposition, leading to the formation of carbon-rich deposits or carbon shells on laser-generated nanoparticles, is widely known for laser fragmentation in organic solvents. [38, 27, 40] Interestingly, the pristine $Ni_{2.25}Co_{6.75}S_8$ already contains approximately 12 at.% carbon and 15 at.% oxygen. Since tetraethylene glycol is used during the ball-milling process, residual or decomposition products derived from this organic compound may contribute to the observed carbon and oxygen contents. Following the laser processing, both elemental fractions increase

progressively with increasing processing intensity. For the 200 mJ/cm² series (Figure S14a), only a slight increase to approximately 17 at.% carbon and 20 at.% oxygen is observed. Since the Ni, Co, and S contents remain essentially unchanged under these conditions, the additional carbon and oxygen are most likely associated with pyrolysis products originating from the decomposition of isopropanol. For the 400 mJ/cm² series, the carbon and oxygen contents increase to approximately 24 and 28 at.%, respectively. For the 600 mJ/cm² series, both elemental fractions increase only moderately up to 48 PPV, followed by a pronounced rise to approximately 40-45 at.% after 72 PPV. As this behavior deviates from the overall trend and the remaining particle fraction in this sample is comparatively low, the values obtained for 72 PPV should be interpreted with caution. Finally, the 800 mJ/cm² series exhibits the highest carbon and oxygen contents, reaching approximately 30 at.% carbon and 40 at.% oxygen after 72 PPV, consistent with the increasing laser fluence and PPV.

To further investigate the nature of the pyrolysis products formed during laser processing, thermogravimetric analysis coupled with evolved gas analysis by GC-MS was performed (Figure S15). First, the appropriate desorption temperature was determined from the TGA curve (Figure S15c). Based on the maximum mass loss associated with the decomposition of the pyrolysis products, a temperature of 275 °C was selected for the subsequent ATD measurements. The GC-MS analysis reveals the formation of several volatile compounds that are absent in the pristine material and therefore originate from the laser treatment. These products can be grouped into three categories. The first comprises compounds originating solely from the pyrolysis of isopropanol (e.g. 2-ethylhexanal). The second includes sulfur-containing species, (e.g. methylthio-2-propanone), indicating that the laser-induced reactions involve not only solvent decomposition but also interactions between isopropanol and the sulfur-containing pentlandite particles. Finally, several silane compounds, such as

hexamethyldisilathiane, are detected. These species most likely originate from the tubing material of the experimental setup and may additionally participate in secondary reactions. The observed product distribution is consistent with previous studies on laser fragmentation in organic liquids, where laser-induced solvent decomposition leads to the formation of reactive radical species that subsequently undergo recombination and secondary reactions, giving rise to a wide range of pyrolysis products. [41–43]

Laser processing in organic liquids has also been reported to induce the formation of carbon shells around nanoparticles. [38, 40, 27] Such graphitic or carbonaceous layers may not decompose under the selected ATD conditions and therefore remain undetected. To investigate the possible presence of carbon shells or carbon incorporated at or within the particles, STEM-EDS line scans were performed on selected samples processed at 400 mJ/cm² 48 PPV and 800 mJ/cm² 48 PPV (Figure 4c). These conditions were chosen to determine whether differences in the carbon distribution correlate with the onset of the enhanced HER activity. Interestingly, the STEM-EDS line scans reveal a clear difference between the two samples. While the 400 mJ/cm² 48 PPV sample exhibits a pronounced increase in the overall carbon content according to the SEM-EDS analysis, the STEM-EDS line scan reveals no pronounced carbon enrichment at the particle surface. This suggests that carbon-containing pyrolysis products are present in the sample but seem not to be deposited specifically on or inside the particles. In contrast, the 800 mJ/cm² 48 PPV sample exhibits a significant carbon signal that starts approximately 1 nm before the particle edge and extends across the entire particle. Although the line scan alone does not allow an unambiguous assignment of the carbon distribution within the particle, the increased carbon intensity at the particle boundary would be consistent with surface carbon enrichment. Previous studies have demonstrated that thin carbon shell features

can positively influence the HER performance of nanocatalysts. Consequently, the surface carbon enrichment identified for the 800 mJ/cm² 48 PPV sample may represent one possible origin of the observed activity enhancement. [34]

As discussed above, the subtle lattice contraction observed by XRD suggests that laser processing may induce structural defects, potentially including sulfur vacancies, which could also contribute to the observed sulfur depletion. To further investigate this hypothesis and to elucidate the origin of the enhanced HER activity, electron paramagnetic resonance (EPR) spectroscopy was performed on the pristine material as well as the selected 400 and 800 mJ/cm² samples processed at 48 PPV (Figure 4d). Interestingly, the pristine $Ni_{2.25}Co_{6.75}S_8$ exhibits no detectable EPR signal, indicating the absence of a significant concentration of paramagnetic species. In contrast, a distinct EPR signal is observed for the 400 mJ/cm² sample, while the 800 mJ/cm² sample exhibits a substantially stronger signal. These results demonstrate that laser processing leads to a progressive increase in the concentration of paramagnetic species. Interestingly, although the overall extent of sulfur depletion determined by SEM-EDS is comparable for the samples processed at 400 and 800 mJ/cm², the latter exhibits a substantially stronger EPR response. Considering that sulfur vacancies are known to enhance HER activity [44, 45], these findings suggest that, despite the similar overall sulfur loss, a larger fraction of the sulfur depletion at higher laser fluences may be associated with the formation of sulfur defects, which could contribute to the observed improvement in catalytic performance. However, the exact nature of the paramagnetic species cannot be unambiguously identified from the present EPR data, as the observed signals may also originate from other structural defects or specific Ni and Co oxidation and coordination states.

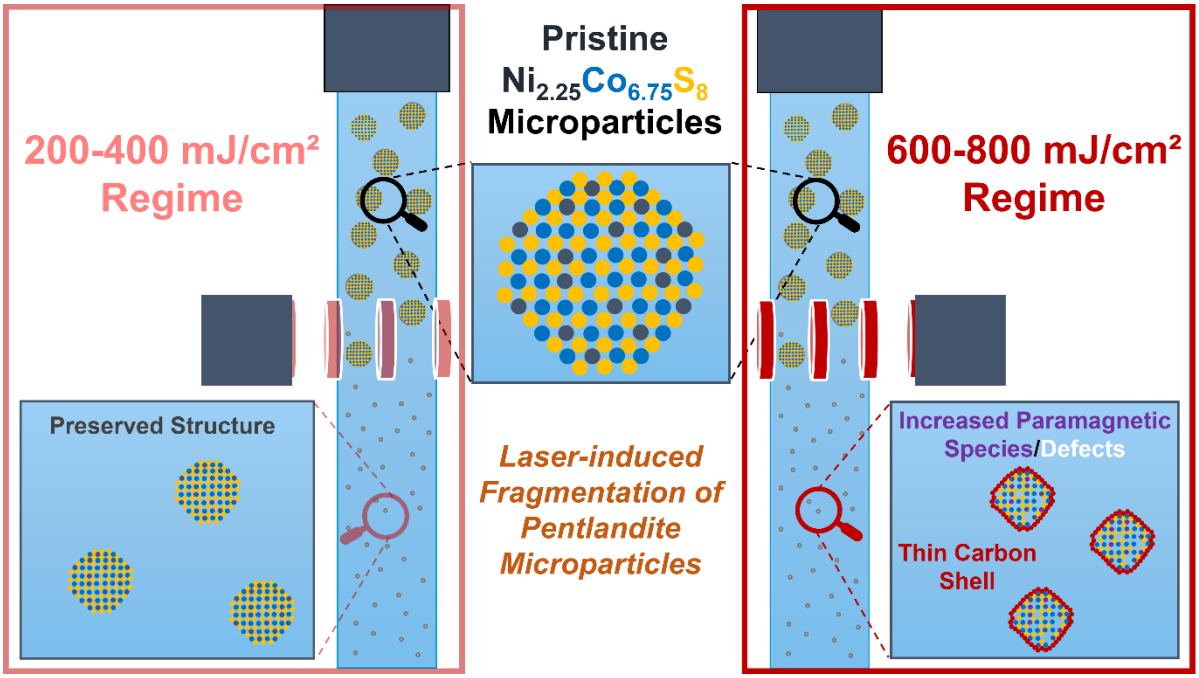


Figure 5: Schematic illustration of the proposed laser-induced evolution of $Ni_{2.25}Co_{6.75}S_8$ pentlandite particles during picosecond laser fragmentation in liquids. Processing at 200-400 mJ/cm² primarily produces nanoparticles with a largely preserved crystal structure, whereas processing at 600-800 mJ/cm² is proposed to additionally induce thin carbon shell formation and an increased concentration of paramagnetic species associated with laser-induced defects.

Taken together, the present results indicate that increasing the accessible surface area through particle size reduction alone is insufficient to enhance the HER activity of pentlandite. While complete fragmentation into nanoparticles is already accomplished at 400 mJ/cm², a significant improvement in HER activity is observed only for samples processed at 600 and 800 mJ/cm². This finding indicates that additional laser-induced material modifications, rather than particle size reduction alone, are responsible for the observed enhancement in catalytic performance. As summarized schematically in Figure 5, fragmentation at relatively low laser fluences (200-400 mJ/cm²) predominantly produces nanoparticles while largely preserving their crystal structure.

In contrast, processing at higher laser fluences (600-800 mJ/cm²) results in the simultaneous formation of a thin carbon shell and a pronounced increase in the concentration of paramagnetic species, indicating a higher density of laser-induced defects. Although the exact nature of these paramagnetic species remains unresolved, the combined experimental evidence suggests that these structural and chemical modifications, represent the only distinguishable material modifications between the 400 and 800 mJ/cm² samples. Since particle size, crystal structure, sulfur depletion, these laser-induced structural and chemical modifications are considered the most likely origin of the enhanced electrocatalytic performance. The proposed mechanism therefore highlights that picosecond laser fragmentation in liquids not only represents an effective nanoparticle fabrication technique but also enables simultaneous nanoscale surface and defect engineering, providing an additional degree of freedom for tailoring the catalytic properties of pentlandite-based electrocatalysts.

Conclusion

Pentlandites are promising electrocatalysts for the HER due to their favorable catalytic performance, earth abundance, and the possibility of directly utilizing the naturally occurring ore as catalyst material. However, conventional synthesis routes typically yield micrometer-sized particles, and further particle size reduction by established mechanical processing methods remains challenging. Transforming these materials into nanoparticles is expected to improve catalyst utilization through a higher accessible surface area and may further enhance the catalytic performance. Therefore, picosecond LFL has emerged as a promising solution, as it has been successfully applied to a wide range of materials while largely preserving their pristine structure. In this work, the impact of laser fluence and induced PPV on the

fragmentation of $Ni_{2.25}Co_{6.75}S_8$ pentlandite microparticles was systematically investigated and correlated with the resulting structural, chemical, and electrochemical properties to identify optimal laser processing conditions for improved HER Performance. Laser processing successfully transformed the pentlandite microparticles into nanoparticles with average particle sizes between 10 and 40 nm. While processing at 200 mJ/cm² resulted in only partial fragmentation of the particle population, fluences of 400 mJ/cm² and above led to essentially complete fragmentation without further significant reductions in particle size. Throughout the investigated parameter range, the crystalline pentlandite structure remained largely preserved, whereas SEM-EDS revealed the onset of sulfur depletion at laser fluences of ≥400 mJ/cm² and ≥48 PPV, indicating compositional modifications. Despite the comparable particle sizes obtained at fluences of 400 mJ/cm² and above, a pronounced enhancement of the HER activity was exclusively achieved for samples processed at 600 and 800 mJ/cm², reaching a maximum overpotential reduction of approximately 50 mV (≈15%) together with improved electrochemical stability in RDE based measurements. These findings clearly demonstrate that size reduction and sulfur depletion alone are insufficient to explain the improved catalytic performance. Instead, the comprehensive characterization suggests that the enhanced HER activity is most likely associated with the formation of a thin carbon shell, as revealed by TEM-EDS, together with an increased concentration of paramagnetic species observed by EPR, indicating a higher density of laser-induced defects within the nanoparticles. Overall, this study demonstrates that picosecond LFL is not merely an effective fragmentation technique but also a versatile post-synthetic tool for tailoring catalyst properties through controlled laser-induced material modifications. Beyond enabling the nanoscale processing of catalyst materials that are inaccessible by conventional size-reduction methods, the presented approach opens new opportunities for the

development and optimization of earth-abundant electrocatalysts and may provide a broadly applicable strategy for future laser-assisted catalyst engineering.

Experimental Section

$Ni_{2.25}Co_{6.75}S_8$ microparticles were synthesized mechanochemically according to previous reports [16] in a Fritsch planetary ball mill using ZrO_2 milling containers and ZrO_2 milling balls. Metal and sulfur powder were used as reactants and milling was performed under inert atmosphere.[46]

Laser Fragmentation in Liquids (LFL) of $Ni_{2.25}Co_{6.75}S_8$ pentlandite microparticles was performed in isopropanol (VWR, 99.9 %) at a microparticle concentration of 1 g/L and continuously redispersed by ultrasonication throughout the laser processing. The suspension was circulated from a reservoir through a round nozzle (Lechler 54436016CA001) using a peristaltic pump (Ismatec RHP100994), forming a free liquid jet that was irradiated under an argon atmosphere to minimize interactions with ambient air. Laser fragmentation was performed using a picosecond laser system (EdgeWave SN1056, 1064 nm, 50 kHz). The laser beam was focused onto the liquid jet using two lenses with focal lengths of 300 mm, delivering a focal spot of 1.45 mm by 0.23 mm. The laser power was adjusted to achieve fluences of 200, 400, 600, and 800 mJ/cm². The transmitted laser power was monitored using a power meter prior to each experiment. The liquid jet exhibited a width of 1.05 mm. A volumetric flow rate of 63 mL/min was employed, corresponding to approximately 12 pulses per volume (PPV) per passage. For each fluence, the suspension was processed for up to six passages corresponding to cumulative irradiation doses of 24, 48, and 72 PPV. Following laser processing, the fragmented particles were recovered by removing the

solvent using a rotary evaporator operated at 60 °C under reduced pressure and 300 rpm.

Rotation Disk Electrode (RDE) Measurements were used to investigate the hydrogen evolution reaction (HER) activity of pristine and laser-fragmented $Ni_{2.25}Co_{6.75}S_8$ samples using a conventional three-electrode electrochemical cell. A glassy carbon (GC) electrode served as the working electrode, a platinum wire as the counter electrode, and an Ag/AgCl (3°M KCl) electrode as the reference electrode. All measurements were performed in 0.5 M H_2SO_4 electrolyte at room temperature. Catalyst inks were prepared by dispersing 5 mg of catalyst powder and 1.6 mg carbon black in a mixture of 162 µL deionized water, 486 µL isopropanol, and 35 µL of a 5 wt% Nafion solution. The suspension was homogenized by ultrasonication prior to deposition. A total volume of 27 µL ink was drop-cast onto the GC electrode in nine consecutive aliquots of 3 µL, with intermediate drying at 60 °C. Electrochemical measurements were conducted using an RDE rotation rate of 1600 rpm to ensure efficient mass transport. Prior to each experiment, the electrodes were electrochemically cleaned by 50 cyclic voltammetry (CV) cycles between 0 and -200 mV vs. reversible hydrogen electrode (RHE). Following catalyst activation, HER polarization curves were recorded by CV between 0 and -500 mV vs. RHE using three consecutive cycles at a scan rate of 5 mV/s, and the third cycle was used for activity evaluation. Long-term HER stability was evaluated by chronoamperometry at -300 mV vs. RHE under continuous electrode rotation at 1600 rpm for 12 h. Double-layer capacitances were determined by recording cyclic voltammograms within a potential window of ±20 mV relative to the open-circuit potential (OCP) at scan rates of 10, 20, 30, 40, and 50 mV/s.

Fabrication of Membrane electrode assemblies (MEAs) was performed as reported previously [46] by spray coating of a Nafion115 membrane with catalyst inks. For the

anode, Nafion D2020 (IonPower, 20 % dispersion in ethanol/ propanol) in 17.7 % relation to commercial IrO_2 powder (Thermo Scientifc) were dispersed in 2-propanol and this ink was applied to the membrane via automatic spray coating with a Sonotek FlexiCoat. Cathode ink was prepared from $Ni_{2.25}Co_{6.75}S_8$ nanoparticles in isopropanol, which were combined with Carbon Vulcan (Quintech) and Nafion D2020 in a mass ratio of 3:1:1, respectively. The dispersion was filled up with ultrapure water to reach an isopropanol:water ratio of 3:1 and subsequently mixed with an Ultra-Turrax at 13500 rpm for 2 min. The as-prepared inks were manually spray-coated on the back side of the IrO_2-coated Nafion membrane using an airbrush spray gun until a catalyst loading of 1 mg/cm² was achieved. The coated electrodes were hot-pressed at 10 bar and 135 °C for 90 s in a Servitec Polystat 300 S hot-press.

Electrochemical Testing in a Zero-Gap Electrolyzer developed by Fraunhofer ISE with Ti felts as porous transport layers was utilized for electrochemical characterization of MEAs. [47] The compression on the 4 cm^2 active area was set to 3 – 5 MPa as deduced from pressure tests prior to electrolysis experiments. Electrolyzer operation was executed under circulation of ultrapure water on the anode side at 100 mL/min with a dry cathode. The temperature at the cell outlet was regulated to 80 °C. After flushing the system for a minimum of 12 h, a short-circuit test was performed followed by conditioning at 1 A/cm^2 and 1.9 V for 30 min each. Subsequently, polarization curves were recorded by 60 s holds of each current density based on the EU harmonized protocol. [48] Data points of the polarization curves represent an average of the voltage measured during the last 30 s of each current density hold with the respective error range deduced from at least two repetitive measurements of different electrodes. Electrochemical impedance spectroscopy was performed at 5 % perturbation amplitude and 10 points per decade in a frequency range of 1 – 40000 Hz in galvanostatic mode.

Gas Chromatographic (GC) coupled Automatic Thermal Desorption (ATD) and Thermo Gravimetric Analysis (TGA) Measurements were performed using PerkinElmer instrumentation. A TurboMatrix 650 thermal desorption unit was coupled to a Clarus 690 gas chromatograph equipped with a Clarus SQ 8C mass spectrometer as the detector. Aliquots of the powdered samples were placed in glass desorption tubes. Glass wool plugs were inserted to prevent sample particles from being carried out of the tubes by the gas flow. Prior to thermal desorption, the tubes were purged with helium for 1 min to remove air. The samples were subsequently desorbed at 275 °C for 10 min using a helium flow of 2 mL/min through the tubes. During thermal desorption, the desorbed compounds were collected and focused in a cold trap maintained at -30 °C. The cold trap was then rapidly heated to 275 °C to transfer the trapped compounds to the GC-MS system. Chromatographic separation was performed using a PerkinElmer Elite-5MS capillary column with a length of 30 m, an internal diameter of 0.25 mm, and a film thickness of 0.25 µm. The outlet split ratio was set to 1:9, resulting in the transfer of 10% of the desorbed analytes onto the GC column. Helium was used as the carrier gas at a column flow rate of 1.2 mL/min. The GC oven was initially maintained at 30 °C. The temperature was then increased to 120 °C at a rate of 8 °C/min, followed by an increase to 220 °C at 20 °C/min. The final temperature was held for 8 min. The mass spectrometer was operated in electron ionization mode at an ionization energy of 70 eV. Mass spectra were acquired in full-scan mode over an m/z range of 30-250. Compounds were tentatively identified by comparison of the acquired mass spectra with reference spectra contained in the NIST 17 Mass Spectral Library.[49]

Transmission Electron Microscopy (TEM) Measurements were performed using a JEOL JEM 1400 Plus and a JEOL JEM 2200FS equipped with a probe-side Cs corrector operated at 200 kV to determine the particle size distribution, morphology,

and elemental composition of pristine and laser-fragmented $Ni_{2.25}Co_{6.75}S_8$ pentlandite samples.

X-Ray Diffraction (XRD) Measurements were employed to analyze the structural integrity, phase composition, and crystallite size of the pristine and LFL processed Nanoparticles. Using a powder X-ray diffractometer (PXRD) (Bruker D8 Advance) equipped with Cu-Kα radiation (λ = 1.5406 Å), measurements were conducted over a 2θ range of 15° - 90° with a step size of 0.02°, a dwell time of 4 s per step, resulting in a total scan duration of 4.5h. Qualitative phase analysis was performed with the software Diffrac.Suite EVA V7.1 (Bruker) with the pattern of $NiCo_2S_4$ (#43-1477), CoS (#75-0605) and Co_9S_8 (#86-2273) from the ICDD database. After instrumental calibration with the reference material LaB6 from NIST (SRM 660b), quantitative Rietveld refinement (using fundamental parameters approach, FPA) was performed with the software TOPAS 7.0 (Bruker) to calculate the lattice parameters and the average crystallite size from diffraction peak broadening. [R_{wp} (pristine $Ni_{2.25}Co_{6.75}S_8$) = 7.53; R_{wp} (400 mJ/cm² 48 PPV) = 6.66; R_{wp} (600 mJ/cm² 24 PPV) = 7.43; R_{wp} (600 mJ/cm² 48 PPV) = 7.01; R_{wp} (600 mJ/cm² 72 PPV) = 6.34; R_{wp} (800 mJ/cm² 48 PPV) = 6.66].

Scanning electron microscopy (SEM) characterization was performed using an Apreo S LoVac microscope (Thermo Fisher Scientific). Samples were prepared by drop-casting the particle suspension onto a silicon single-crystal substrate and subsequently dried under ambient conditions. Energy-dispersive X-ray spectroscopy was performed with a Thermo Scientific UltraDry silicon drift X-ray detector coupled to the microscope.

Electron Paramagnetic Resonance (EPR) spectroscopy Measurements were performed at room temperature using a Bruker Magnettech ESR5000 benchtop spectrometer (field range: 25-625 mT, modulation amplitude: 0.7 mT, microwave power: 0.01 mW, sweep time: 180 s). Low-temperature measurements (20 K) were

conducted on a Bruker Elexsys E500 (X-band) spectrometer equipped with an ER4116DM resonator and an Oxford ESR900 cryostat (field range: 20-1000 mT, modulation amplitude: 0.7 mT, microwave power: 1 mW, sweep time: 204.82 s). Spectral simulations were performed using the EasySpin toolbox (Matlab) with the “pepper” function. [50]

Supporting Information

Calculation of Pulses per Volume and Laser Fluence; Picosecond IR Laser Intensity Profile; TEM Particle Size Distributions; Hydrogen Evolution Reaction (HER) Measurements; X-ray Diffraction (XRD) Analysis; Elemental Composition Analysis by SEM-EDS; Identification of Pyrolysis Products by TGA-ATD-GC-MS; Global Particle Size Distribution by Analytical Centrifugation.

Acknowledgement

P.L. gratefully acknowledges financial support from the Deutsche Bundesstiftung Umwelt (DBU) through a doctoral scholarship. The authors gratefully acknowledge Stephan Barcikowski for the original idea that inspired this work, which emerged during a coffee-break discussion in Mülheim an der Ruhr. The authors acknowledge financial support under Project 388390466 – TRR 247 and the support by the Interdisciplinary Center for Analytics on the Nanoscale (ICAN) of the University of Duisburg-Essen (DFG-RIsources reference: RI_00313), a DFG-registered core facility (Project Nos. 233512597 and 324659309). We gratefully acknowledge Alexander Schnegg for providing access to the EPR spectrometer funded by the SFB 247 (project 388390466) and Takuma Sato for carrying out the EPR measurements. The instrumentation used for the ATD-GC-MS measurements was funded by the German

Research Foundation (DFG) under grant no. INST 20876/448-1 FUGG. J.W. gratefully acknowledges financial support from the Studienstiftung des Deutschen Volkes. U. P. A. acknowledges funding by the Deutsche Forschungsgemeinschaft (DFG, German Research Foundation) under Germany's Excellence Strategy – EXC 2033, Project-ID 390677874-RESOLV.

References

1. Alzoubi, A. *Int. J. CIM* **2021,** *1* (1).
2. Kourougianni, F.; Arsalis, A.; Olympios, A. V.; Yiasoumas, G.; Konstantinou, C.; Papanastasiou, P.; Georghiou, G. E. *Renewable Energy* **2024,** *231*, 120911.
3. Osman, S. H.; Mat Yatim, N. S.; Jehan Elham, O. S.; Shaari, N.; Zakaria, Z. *Sustainable Energy Fuels* **2025,** *9* (12), 3182–3202.
4. Israr, A.; Saadat, M.; Israr, A.; Rehman, A.; Junaid, M. *Sustainable Energy Technologies and Assessments* **2026,** *86*, 104886.
5. Carmo, M.; Fritz, D. L.; Mergel, J.; Stolten, D. *International Journal of Hydrogen Energy* **2013,** *38* (12), 4901–4934.
6. Ayers, K. E.; Anderson, E. B.; Capuano, C.; Carter, B.; Dalton, L.; Hanlon, G.; Manco, J.; Niedzwiecki, M. *ECS Trans.* **2010,** *33* (1), 3–15.
7. GRIGORIEV, S.; POREMBSKY, V.; FATEEV, V. *International Journal of Hydrogen Energy* **2006,** *31* (2), 171–175.
8. Smialkowski, M.; Siegmund, D.; Stier, K.; Hensgen, L.; Checinski, M. P.; Apfel, U.-P. *ACS Materials Au* **2022,** *2* (4), 474–481.
9. Smialkowski, M.; Tetzlaff, D.; Hensgen, L.; Siegmund, D.; Apfel, U.-P. *Chinese Journal of Catalysis* **2021,** *42* (8), 1360–1369.

10. Konkena, B.; junge Puring, K.; Sinev, I.; Piontek, S.; Khavryuchenko, O.; Dürholt, J. P.; Schmid, R.; Tüysüz, H.; Muhler, M.; Schuhmann, W.; Apfel, U.-P. *Nat Commun* **2016,** *7* (1), 12269.
11. Xia, F.; Pring, A.; Brugger, J. *Minerals Engineering* **2012,** *27-28*, 11–19.
12. Amin, H. M. A.; Attia, M.; Tetzlaff, D.; Apfel, U.-P. *ChemElectroChem* **2021,** *8* (20), 3863–3874.
13. Bentley, C. L.; Andronescu, C.; Smialkowski, M.; Kang, M.; Tarnev, T.; Marler, B.; Unwin, P. R.; Apfel, U.-P.; Schuhmann, W. *Angewandte Chemie International Edition* **2018,** *57* (15), 4093–4097.
14. Liu, H.; Tian, Y.; Lenus, S.; Zhao, X.; Dai, Z.; Liang, T. *Mater. Adv.* **2024,** *5* (5), 1892–1896.
15. Kim, Y.; Karuppannan, M.; Lee, D.; Bae, H. E.; Luong, Q. T.; Kang, S. Y.; Sung, Y.-E.; Cho, Y.-H.; Kwon, O. J. *Intl J of Energy Research* **2022,** *46* (3), 3145–3154.
16. Tetzlaff, D.; Pellumbi, K.; Baier, D. M.; Hoof, L.; Shastry Barkur, H.; Smialkowski, M.; Amin, H. M. A.; Grätz, S.; Siegmund, D.; Borchardt, L.; Apfel, U.-P. *Chem. Sci.* **2020,** *11* (47), 12835–12842.
17. Zhang, D.; Gökce, B.; Barcikowski, S. *Chemical Reviews* **2017,** *117* (5), 3990–4103.
18. Ziefuß, A. R.; Reichenberger, S.; Rehbock, C.; Chakraborty, I.; Gharib, M.; Parak, W. J.; Barcikowski, S. *J. Phys. Chem. C* **2018,** *122* (38), 22125–22136.
19. Lau, M.; Barcikowski, S. *Applied Surface Science* **2015,** *348*, 22–29.
20. Friedenauer, T.; Buck, K.; Eberwein, M.; Bünte, A.-L.; Rehbock, C.; Barcikowski, S. *Part & Part Syst Charact* **2023,** *40* (12), 2300034.
21. Friedenauer, T.; Spellauge, M.; Sommereyns, A.; Rehbock, C.; Huber, H. P.; Barcikowski, S. *J. Phys. Chem. C* **2025,** *129* (14), 6803–6816.

22. Spellauge, M.; Tack, M.; Streubel, R.; Miertz, M.; Exner, K. S.; Reichenberger, S.; Barcikowski, S.; Huber, H. P.; Ziefuss, A. R. *Small* **2023,** *19* (10), e2206485.
23. Yu, M.; Waag, F.; Chan, C. K.; Weidenthaler, C.; Barcikowski, S.; Tüysüz, H. *ChemSusChem* **2020,** *13* (3), 520–528.
24. Ziefuss, A. R.; Stratmann, N.; Reifenrath, C.; Kanu, G.; Berndt, N.; Disch, S.; Barcikowski, S. *Opt. Lett., OL* **2026,** *51* (2), 437–440.
25. Ziefuß A. R.; Tibbetts K. M.; Barcikowski S. *Handbook of Green Laser Synthesis & Processing of Colloids*, 2025.
26. Koch, N. G.; Poschmann, M.; Heumann, S.; Puthussery, A. J.; Čolić, V.; Barcikowski, S.; Reichenberger, S. *ChemCatChem* **2025,** *17* (16), e00622.
27. Nallathambi, V.; Kim, S.-H.; Mingers, A. M.; Ebbinghaus, P.; Gault, B.; Reichenberger, S.; Raabe, D.; Barcikowski, S. *Advanced Science* **2026,** *13* (1), e10537.
28. Spellauge, M.; Tack, M.; Streubel, R.; Miertz, M.; Exner, K. S.; Reichenberger, S.; Barcikowski, S.; Huber, H. P.; Ziefuss, A. R. *Small* **2023,** *19* (10), e2206485.
29. Krenz, L.; Fromme, T.; Tibbetts, K. M.; Barcikowski, S.; Ziefuss, A. R. *J. Phys. Chem. C* **2026,** *130* (11), 4080–4088.
30. Lemm, P.; Söder, J.; Reichenberger, S.; Barcikowski, S. *Adv Energy and Sustain Res* **2026,** *7* (1), e202500242.
31. Li, Z.; Fu, J.-Y.; Feng, Y.; Dong, C.-K.; Liu, H.; Du, X.-W. *Nat Catal* **2019,** *2* (12), 1107–1114.
32. Schellenburg, D.; Bihnam, T.; Placke-Yan, C.; Bendt, G.; Prymak, O.; Sato, T.; Jennings, D.; Leiva-Leroy, C.; Zhang, D.; Nachev, M.; Dhaka, K.; Nkou, F.; Hagemann, U.; Heidelmann, M.; Kenmoe, S.; Exner, K. S.; Sures, B.; Muhler, M.; Liebscher, C. H.; Schnegg, A.; Schulz, S.; Barcikowski, S.; Reichenberger, S. *ChemCatChem* **2026,** *18* (1), e01054.

33. Matten, M.; Koch, N. G.; Caidi, A.; Radev, I.; Lange, T.; Barcikowski, S.; Reichenberger, S. *J. Phys. Chem. C* **2025,** *129* (16), 7740–7750.
34. Ahn, H.; Senthil, R. A.; Jung, S.; Kumar, A.; Ubaidullah, M.; Choi, M. Y. *eScience* **2025,** *5* (5), 100408.
35. J. Wierper, R. Guerra, K. Pellumbi, J. Jökel, U.-P. Apfel. *Int. J. Hydrog. Energy* **2026**, Submitted.
36. Bornet, A.; Moreno-García, P.; Dutta, A.; Kong, Y.; Liechti, M.; Vesztergom, S.; Arenz, M.; Broekmann, P. *ACS Catalysis* **2024,** *14* (23), 17331–17346.
37. Lazaridis, T.; Stühmeier, B. M.; Gasteiger, H. A.; El-Sayed, H. A. *Nat Catal* **2022,** *5* (5), 363–373.
38. Stuckert, R.; Pohl, F.; Prymak, O.; Schürmann, U.; Rehbock, C.; Kienle, L.; Barcikowski, S. *Beilstein J. Nanotechnol.* **2025,** *16* (1), 1141–1159.
39. Lemm, P.; Maier, K.; Prymak, O.; Stuckert, R.; Mockenhaupt, B.; Sato, T.; Barcikowski, S. *Colloids and Surfaces A: Physicochemical and Engineering Aspects* **2026,** *748*, 140996.
40. Fromme, T.; Reichenberger, S.; Tibbetts, K. M.; Barcikowski, S. *Beilstein J. Nanotechnol.* **2024,** *15* (1), 638–663.
41. Fromme, T.; Müller, R.; Krenz, L.; Tintrop, L. K.; Sanjuán, I.; Schmidt, T. C.; Tibbetts, K. M.; Andronescu, C.; Reichenberger, S.; Barcikowski, S. *J. Phys. Chem. C* **2025,** *129* (6), 2953–2965.
42. Fromme, T.; Tintrop, L. K.; Reichenberger, S.; Schmidt, T. C.; Barcikowski, S. *ChemPhysChem* **2023,** *24* (11), e202300089.
43. Harris, S.; Kaplan, E.; Aftel, M.; Tibbetts, K. M. *The journal of physical chemistry. B* **2024,** *128* (42), 10481–10491.
44. Li, Y.; Jiang, C.; Yang, Y.; Zhang, C.; Xu, J.; Zeng, Y.; Yu, S.; Tian, H.; Zheng, W. *Applied Surface Science* **2022,** *604*, 154470.

45. Liu, Y.; Cai, C.; Zhu, S.; Zheng, Z.; Li, G.; Chen, H.; Li, C.; Sun, H.; Chou, I.-M.; Yu, Y.; Mei, S.; Wang, L. *Small* **2024,** *20* (30), e2311161.
46. Wierper, J.; Hiltrop, J.; Pellumbi, K.; Jökel, J.; Sanden, S.; Kożusznik, M.; Mikuła, A.; Apfel, U.-P. *ChemPhysChem* **2025,** *26* (6), e202401015.
47. Lickert, T.; Fischer, S.; Young, J. L.; Klose, S.; Franzetti, I.; Hahn, D.; Kang, Z.; Shviro, M.; Scheepers, F.; Carmo, M.; Smolinka, T.; Bender, G.; Metz, S. *Applied Energy* **2023,** *352*, 121898.
48. Malkow T.; Pilenga A.; Tsotridis G. *EU harmonised polarisation curve test method for low-temperature water electrolysis;* Publications Office of the European Union: Luxembourg, 2018.
49. Stein S. E.; Mirokhin, Y.; Tchekhovskoi, D.; Mallard W.; National Institute of Standards and Technology. NIST/EPA/NIH Mass Spectral Library (NIST 17); National Institute of Standards and Technology: Gaithersburg, MD, USA, 2017.
50. Stoll, S.; Schweiger, A. *Journal of Magnetic Resonance* **2006,** *178* (1), 42–55.